Computational Insights into Hydrogen Interaction with the Ru $(10\bar{1}1)$ and Ru $(10\bar{1}0)$ Surfaces: Implications for Alkane and Polyolefin Hydrogenolysis

Fabio Colasuonno[a], Sohaib Umer[a], and Martina Lessio*[a]
[a]School of Chemistry, The University of New South Wales, Sydney, NSW 2052, Australia
*Corresponding author

Abstract

Hydrogen interaction with transition metal surfaces such as those exposed by ruthenium (Ru) nanoparticles is critical in applications like hydrogen storage and catalytic processes such as Fischer-Tropsch, Haber-Bosch, and plastic waste hydrogenolysis. While the Ru (0001) surface is well-studied, hydrogen interaction with the Ru $(10\bar{1}1)$ and Ru $(10\bar{1}0)$ facets remains mostly underexplored. In this contribution, we use density functional theory calculations to investigate hydrogen adsorption and dissociation and provide insights into the adsorbed hydrogen role in catalytic polyolefin plastic hydrogenolysis. We start our investigation by exploring all the unique surface and subsurface sites for hydrogen adsorption and dissociation and identify hcp and higher hollow as the most favorable atomic hydrogens adsorption sites on the Ru $(10\bar{1}1)$ and Ru $(10\bar{1}0)$ surfaces, respectively. We find that atomic hydrogen can easily migrate on these surfaces to achieve the most stable arrangement at different coverages. We then combine these findings with ab-initio thermodynamics and microkinetic modeling to build surface phase diagrams, which show that both surfaces are fully hydrogenated under typical catalytic conditions. We then study how the presence of the full hydrogen coverage affects the adsorption and dehydrogenation of butane as a proxy for polyethylene, as these are the initial steps in the catalytic hydrogenolysis of polyolefin plastic waste. We find that the adsorption energy of butane decreases when the two surfaces are fully hydrogenated but adsorption remains favorable. We then investigate two possible mechanisms for the dehydrogenation step. The

most favorable dehydrogenation mechanism involves the reaction of a surface hydrogen with an alkane hydrogen to produce H_2 gas and an adsorbed alkyl radical. However, both mechanisms have positive reaction free energies suggesting that polyolefin dehydrogenation will be slow on these surfaces.

Introduction

The investigation of the interactions between hydrogen and metal surfaces is an important and growing research field due to its multiple possible applications, spanning from hydrogen storage to catalysis. Specifically, in the field of catalysis, Ru nanoparticles have demonstrated outstanding performances in multiple reactions that use hydrogen gas such as the Haber-Bosch process, the Fischer-Tropsch process, and, in the last decade, the chemical conversion of plastic waste to fuels via hydrogenolysis.[1–8] Nanoparticles typically expose a plethora of facets, some more prominent than others depending on their surface energy; however, specific facets can be selectively grown by engineering the synthetic process and tune the reactivity of the nanoparticle.[9–13] In fact, different facets can have very different chemistry and catalytic capability. Thus, in the context of catalytic reactions using hydrogen, an understanding of the interactions of these surfaces with H_2 and their hydrogen coverage under operating conditions is needed. The hydrogen coverage can alter the surface chemistry and consequently the catalytic ability of the surface.

The most exposed surface for hcp Ru nanoparticles is the (0001) which is the most stable one and is always exposed, for this reason it has been widely investigated experimentally and computationally.[14–17] In a recent study by our group, we used ab-initio thermodynamics and kinetics to investigate the hydrogen coverage of this surface under different conditions of H_2 pressure and temperature, ranging from STM conditions to catalytic conditions relevant to polyolefin plastic waste hydrogenolysis.[18] The $(10\bar{1}1)$ and the $(10\bar{1}0)$ facets are also always

exposed, despite to a lesser extent, as they constitute the edges of Ru nanoparticle as demonstrated by the calculated Wulff shape for Ru.[19] Furthermore, their exposure can be enhanced via specific synthetic protocols and this has been shown to lead to higher catalytic activity towards reactions such as the hydrogen evolution reaction and the oxygen evolution reaction.[9,20–23]

In this work, we aim to study the hydrogen coverage on the $(10\bar{1}1)$ and the $(10\bar{1}0)$ surfaces of Ru under typical catalytic conditions for polyolefin plastic waste hydrogenolysis, a relatively new application of supported Ru nanoparticles. During hydrogenolysis, the large H_2 pressures lead to the formation of atomic surface hydrogens that react with the plastic polymer to break down the polymeric chain. In order to study these processes, we start our investigation focusing on the interaction between hydrogen and the investigated surfaces. Specifically, we analyze all the possible adsorption surface sites for both atomic and molecular hydrogen to identify the most stable ones; as part of this analysis, we investigate occupation of subsurface sites for atomic hydrogen. In addition, we also characterize the energetics for atomic hydrogen to hop in between the most stable sites and diffuse on the surface. We then move on to study the effect of the atomic hydrogen coverage on the dissociation energy of molecular hydrogen to establish whether the buildup of atomic hydrogen can prevent further H_2 dissociation leading to submonolayer coverage. Finally, we use ab-initio thermodynamics and microkinetic modelling to compute atomic hydrogen surface coverage phase diagrams that allow us to identify the most stable atomic hydrogen coverage under different conditions of H_2 pressure and temperature. We find that the investigated surfaces are both characterized by a full atomic hydrogen surface coverages under catalytic conditions. We thus explore the effect of these surface conditions on the initial steps that ultimately lead to C-C cleavage, specifically adsorption and dehydrogenation; to this end, we use butane as a proxy for polyethylene.

Methods

Computational approach

All calculations were performed using the periodic Vienna Ab-initio Simulation Package (VASP) 6.3.2[24–26]. The Perdew-Burke-Ernzerhof (PBE) functional[27] with the D3BJ dispersion scheme[28,29] has been adopted throughout all the calculations. Nuclei and frozen core electrons were modelled using the projector augmented wave (PAW) scheme from VASP[30] while valence electrons were modelled with plane waves with a 400 eV energy cut-off. A 4×4×1 Γ-centered Methfessel-Paxton grid was selected for k-points sampling for all the surface calculations, while for butane and hydrogen molecules only the Γ point was sampled. We selected a first-order Methfessel-Paxton smearing method with a smearing width of 0.2 eV for all the geometries involving the surface; for butane and hydrogen molecules a gaussian smearing method was used with a small smearing width of 0.001 eV in order to simulate the sharp difference between the occupied and unoccupied energy levels in molecules. Structures were optimized until the maximum force on each atom was less than 0.03 eV/Å. To verify that the optimized geometries represent actual minimum points on the potential energy surface, frequency calculations were carried out for all atoms belonging to the adsorbates as well as the first layer of the slab as this strategy represents a good balance between computational cost and accuracy as shown in Section S1 of the Supporting Information. Thermochemistry corrections to the electronic energies (E) were derived from the frequencies calculations and used to compute free energies (G) as shown in Equation 1:

$$G = E + ZPE + H(T) - T \cdot S(T) \quad (1)$$

where $H(T)$ and $T \cdot S(T)$ are the enthalpic and entropic corrections at temperature T and ZPE is the zero point energy correction.

The Nudged Elastic Band (NEB) algorithm as implemented in the Vienna Transition State Tools (VTST) package for VASP was utilized for transition state (TS) searches.[31] Furthermore, we refined and checked the TS structures derived with the NEB method utilizing the dimer algorithm from the same package.[32] A stricter force convergence criteria than the one for the optimization was selected for the TS optimization and set to 0.01 eV/Å for both the NEB and dimer methods. All TS structures were confirmed to be an actual saddle point on the potential energy surface by performing a frequency analysis and ensuring that only one imaginary frequency was found. These results were also used to calculate G of the TS structures (according to Equation 1) and derive the corresponding activation free energies.

Surfaces were modelled using a 4×4 supercell (a=10.93 Å and b=9.85 Å) for the $(10\bar{1}1)$ surface and a 3×2 supercell (a=8.04 Å and b=8.49 Å) for the $(10\bar{1}0)$ to be able to simulate a variety of hydrogen coverages. The slab thickness was set to three layers based on convergence tests (see Section S1 of the Supporting Information) and the bottom layer was kept frozen to simulate the effect of the bulk. In order to avoid self-interaction between slabs, we added 15 Å of vacuum space above the surface. Asymmetric unit cells were adopted for both surfaces, with adsorbates simulated only on the side of the slab allowed to relax. Therefore, we added dipole corrections in the direction orthogonal to the surface. To benchmark our surface models, we compared our calculated surface energy values (as shown in Section S2 in the Supporting Information) with previously computed data available in the literature. Our methodology confirms the trend observed in the literature with the only differences being imputable to the different choice of computational method.

Ab initio thermodynamics

Similarly to our previous work on the Ru (0001) surface,[18] we utilize ab initio thermodynamics to compute surface phase diagrams that depict the most thermodynamically stable atomic hydrogen coverage resulting from the direct dissociation of H_2, defined as in

Equation 2, on the Ru $(10\bar{1}1)$ and the Ru $(10\bar{1}0)$ surfaces under various conditions of temperature and H_2 pressure.

$$H_2(g) + 2* \rightarrow 2\,H^* \tag{2}$$

where $*$ are empty surface sites, and H^* represents adsorbed atomic hydrogen.

In order to obtain the aforementioned phase diagrams, we need to calculate the formation energies for each coverage resulting from different numbers of H_2 molecules directly dissociating on the bare surface from gas phase (ΔG_f), leading to the formation of different surface coverages, as described by Equation 3:

$$\Delta G_f = G_{xH^*} - G_{Ru} - \frac{x}{2}\mu_{H_2}(T, p_{H_2}) \tag{3}$$

where x represents the number of H* adsorbed in the unit cell, G_{xH^*} is the free energy of the surface with x H*, G_{Ru} denotes the free energy of the bare Ru surface, while μ_{H_2} is the chemical potential of H_2. The effects of varying H_2 pressures and temperatures in the experiments have been included by using $\mu_{H_2}(T, p_{H_2})$ calculated as in Equation 4:

$$\mu_{H_2}(T, p_{H_2}) = E_{H_2} + \tilde{\mu}_{H_2}(T, p^0) + k_B T \ln\frac{p_{H_2}}{p^0} \tag{4}$$

in which E_{H_2} represents the electronic energy of H_2 with an added ZPE correction, T denotes the temperature, while k_B the Boltzmann constant. The values for $\tilde{\mu}_{H_2}(T, p^0)$ have been derived from the JANAF-NIST thermochemistry tables adopting the methodology described by Sholl.[33] The $k_B T \ln\frac{p_{H_2}}{p^0}$ term is included to account for the H_2 pressure (p_{H_2}) contribution, with p^0 being a reference H_2 pressure, for simplicity assumed to be standard pressure (*i.e.,* 1 bar).

By plotting ΔG_f vs. μ_{H_2}- $\mu_{H_2}(T, p_{H_2})$, with μ_{H_2} being $\mu_{H_2}(T, p_{H_2})$ evaluated at 0 K and 1 bar, surface phase diagrams were obtained. For each of these plots, the H_2 pressure was fixed, and the temperature was varied across a range (refer to Figure S1 of the Supporting Information) to determine the most stable coverage, defined as the one with the most negative

ΔG_f under the given conditions. This process has been explained in detail in our previous work.[18]

In addition to the cumulative direct dissociation energy ΔG_f, we calculated the stepwise direct dissociation free energy (ΔG_{Diss}) to assess the effect of H* coverage on the H_2 dissociation favorability. ΔG_{Diss} is calculated as follows:

$$\Delta G_{Diss} = G_{\theta}^{ZPE} - G_{\theta'}^{ZPE} - G_{H_2}^{ZPE} \quad (5)$$

Where G_{θ}^{ZPE} is the ZPE corrected free energy of a Ru surface at θ H* coverage, $G_{\theta'}^{ZPE}$ is the ZPE corrected free energy of a Ru surface at θ' H* coverage (which is the starting hydrogen coverage plotted in Figure 1) with $\theta = \theta' + 2\ H^*$, and $G_{H_2}^{ZPE}$ is the ZPE corrected free energy of a gas phase hydrogen molecule.

Microkinetic modeling

The thermodynamic study is completed with a microkinetic analysis in which rate constants for each step are used to calculate the rate of the overall process, and by solving the associated differential equations the concentration of each species is obtained at different temperatures and H_2 pressures. For this purpose we followed the procedure used by Lopez et al. to study the hydrogen coverage on MXene materials.[34] Specifically, the barrierless Hertz-Knudsen equation is used to determine H_2 gas dissociative adsorption rate constant (k_{ads}) as shown in Equation 6:

$$k_{ads} = \frac{p_{H_2} A S}{2\pi m k_B T} \quad (6)$$

where p_{H_2} is the H_2 pressure in bar, A is the area of a single adsorption site calculated as the total area of the surface model divided by the number of possible active sites (i.e., 16 on the $(10\bar{1}1)$ surface, and 12 on the $(10\bar{1}0)$ surface), S is the sticking coefficient for which we adopted a value of 0.001 in order to describe the observed high sticking probability,[35,36] and m is the mass of H_2. On the other hand, the rate constant for H* associative desorption to give H_2

gas (k_{des}) has been computed by means of the Hertz-Knudsen equation for activated processes as shown in Equation 7:

$$k_{des} = \frac{k_B T^3}{h^3} \frac{A(2mk_BT)}{\sigma\, \theta_{rot}} e^{-\frac{G_{des}}{k_BT}} \quad (7)$$

where h is the Planck constant, σ is the symmetry number for H_2, θ_{rot} is the rotational temperature for H_2, and G_{des} is the desorption free energy calculated as:

$$G_{des} = G_{H_2} + G_{2*} - 2G_{H^*} \quad (8)$$

The microkinetic simulations were carried out using the MKMCXX program,[37] employing an H_2 gaseous environment with a total H_2 pressure ranging from 0.1 bar to 100 bar, and temperatures from 100 K to 2000 K. For an example of the obtained output for a specific H_2 pressure refer to Section S4 of the Supporting Information.

Results and Discussion

Surface hydrogen coverage under experimental catalytic conditions

We started our study by investigating the most stable surface sites for H_2 and atomic hydrogen adsorption. Surface site definitions are provided in Figure S3 and adsorption energy results are summarized in Table S7 and S8 of the Supporting Information. For both the $(10\bar{1}1)$ and $(10\bar{1}0)$ surfaces, the only stable adsorption site for H_2 adsorption is the higher top; all the other explored sites led to spontaneous dissociation upon optimization. On the $(10\bar{1}1)$ surface, the most stable site for H* is the hcp site, followed by the fcc site, and then the fourfold hollow site. On the $(10\bar{1}0)$ surface, atomic hydrogen prefers to adsorb on the higher hollow site, closely followed by the higher bridge (less then 0.01 eV difference in adsorption energy), meaning that both sites are likely to be occupied.

In addition to the surface sites, we also investigated subsurface sites occupation inspired by findings widely reported for Pd and its alloys as hydrogen storage materials.[38] In particular, we tested the octahedral site for both surfaces given that it has been reported to be the most

stable subsurface site for Ru;[39] this site is located underneath the highly stable hcp and fcc sites on the $(10\bar{1}1)$ surface and higher hollow and higher bridge sites on the $(10\bar{1}0)$ surface (Figure S6 in the Supporting Information). For the $(10\bar{1}1)$ surface, we also tested the tetragon pyramidal one, which is located underneath the highly stable fourfold hollow sites. All the investigated cases have either a positive reaction energy for the migration of H* from a surface to the subsurface site located underneath or the subsurface H* spontaneously migrates to the surface upon optimization. Specifically, for the octahedral site we found that the subsurface H* spontaneously migrates to the surface on the bare $(10\bar{1}1)$ surface, while the reaction energy for the surface $\rightarrow$ subsurface migration is 0.96 eV on the bare $(10\bar{1}0)$ surface. The $(10\bar{1}1)$ tetragon pyramidal subsite was also found to be unstable upon optimization. Previous studies have shown that a higher hydrogen surface coverage can increase the favorability of subsurface migration on the Ru (0001) surface.[39–41] Therefore, we calculated the surface $\rightarrow$ subsurface migration reaction energy starting from a surface fully covered in H* and moving one H* from a surface site to the one directly underneath it. On the $(10\bar{1}1)$ surface, the subsurface H* occupying an octahedral site no longer spontaneously migrates to the corresponding surface site but the subsurface site occupation remains non-favorable with a surface $\rightarrow$ subsurface migration reaction energy of 0.18 eV; for the tetragon pyramidal subsite, the subsurface H* spontaneously migrates to the corresponding surface fourfold hollow site while displacing the H* nearby to a bridge site. For the fully covered $(10\bar{1}0)$ surface, the surface $\rightarrow$ subsurface migration reaction energy towards an octahedral site is slightly more favorable than on the bare surface, with a reaction energy of 0.77 eV. Overall, based on these results, we concluded that subsurface site occupation of hydrogen atoms does not need to be considered for the $(10\bar{1}1)$ and $(10\bar{1}0)$ surfaces of Ru.

We then proceeded to study the energetics for H_2 dissociation at the surfaces and how it is affected by H* coverage based on our findings for the (0001) surface showing a strong effect

of H* coverage on the H_2 adsorption and dissociation energetics. To this end, we first generated different H* coverages spanning from 0 ML to 1 ML, and for each coverage we established the most favorable arrangement of atoms as reported in Figure S4 and S5 in the Supporting Information. We modeled the dissociation of H_2 as direct dissociation from gas phase (see Equation 2) rather than a two-step process with H_2 adsorption followed by dissociation like we did in our previous work on the (0001) surface. This is based on our findings showing that H_2 molecular adsorption can only occur on the higher top sites while dissociation on all the remaining surface sites is not only spontaneous upon optimization but also significantly more favorable (at least 0.4 eV, see Table S7 and S8 in the Supporting Information).

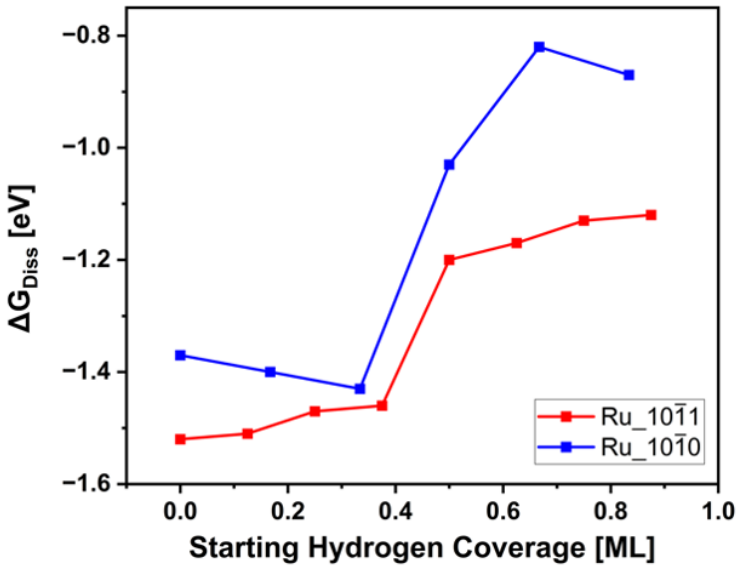

Figure 1: H_2 direct dissociation energy (ΔG_{Diss}) in eV as a function of the starting atomic hydrogen coverage (i.e., the coverage before the dissociation reaction) reported in monolayers (MLs) for the Ru $(10\bar{1}1)$ and $(10\bar{1}0)$ surfaces. Energies are reported at 0 K with ZPE corrections.

The H_2 direct dissociation energy (ΔG_{Diss}, defined in Equation 5) shows an overall increasing trend as a function of H* coverage on both the investigated surfaces (Figure 1, raw data reported in Table S9 and Table S10 in the Supporting Information). More specifically, ΔG_{Diss} has a flat trend up to 0.375 ML for the $(10\bar{1}1)$ surface and 0.333 ML $(10\bar{1}0)$ surface

with a subsequent increase of 0.29 eV and 0.37 eV, respectively. These results can be explained based on different sites being occupied at different coverages. For the $(10\bar{1}1)$ surface, H* exclusively occupies hcp sites for starting coverages up to 0.375 ML. Once the coverage reaches 0.5 ML, there are no more hcp sites available and the fcc sites are in too close proximity to be occupied, causing the fourfold hollow sites to be occupied. Since the fourfold hollow sites are less stable than the hcp we observe a sharp increase in the dissociation energy. For the $(10\bar{1}0)$ surface, H* occupies the higher bridge sites for starting coverages up to 0.334 ML and the direct dissociation energy shows a slight decrease as a function of coverage, indicating attractive lateral H-H interactions. When the starting coverage reaches 0.5 ML, all the newly adsorbed hydrogen atoms occupy higher hollow sites progressively displacing the H* previously sitting on the nearby higher bridge sites to higher hollow sites due to the strong lateral repulsion occurring between H* on close sites; at 1 ML coverage all H* occupy higher hollow sites. When comparing results across the two surfaces, we observe that H_2 dissociation is consistently more favorable on the $(10\bar{1}1)$ surface than on the $(10\bar{1}0)$ surface. This difference can be promptly explained with a comparison of the average H* coordination number (CN) across its adsorption sites at 1 ML of H* coverage on the two surfaces: the average H* CN on the $(10\bar{1}1)$ surface (4.66) is lower than on the $(10\bar{1}0)$ surface (5.5), indicating a stronger driving force for the $(10\bar{1}1)$ H* adsorption sites to be saturated by hydrogen.

Overall, we found that for both the $(10\bar{1}1)$ and the $(10\bar{1}0)$ surface ΔG_{Diss} depends on H* coverage and it becomes less favorable for coverages > 0.5 ML due to different sites being occupied. However, a large driving force for H_2 dissociation is consistently observed for all coverages, with dissociation spontaneously occurring upon optimization. This behavior is very different from what we observed on the (0001) surface in our previous work, for which H_2 adsorption does not occur spontaneously once the H* coverage reaches 0.875 ML meaning that

a full monolayer of atomic hydrogen cannot be achieved on this surface.[18] Given how favorable H_2 dissociation is on the $(10\bar{1}1)$ and $(10\bar{1}0)$ surfaces, we checked the stability of coverages above 1 ML. For both surfaces, dissociation does not occur spontaneously upon optimization at 1 ML; however, it is still energetically favorable over the Ru $(10\bar{1}1)$ surface (ΔG_{Diss} = -0.56 eV) while it is not favorable for the $(10\bar{1}0)$ surface (ΔG_{Diss} = 0.27 eV).

Once H_2 dissociates on a surface, the resulting H* may need to diffuse over the surface to reach the most stable configuration. We therefore studied the energetics of H* diffusion between the most stable surface sites identified earlier in this study. In particular, for the $(10\bar{1}1)$ surface, we identified two migration pathways for H* atoms to diffuse between hcp sites: hcp site → fcc site → hcp site and hcp site → fourfold hollow site → fcc site → hcp site (Figure 2a). We therefore calculated the activation energies for hcp site → fcc site, hcp site → fourfold hollow site, and fourfold hollow → fcc site diffusion at different H* coverages (Table 1). Backward activation energies were also calculated as H* might first adsorb at fcc and fourfold hollow sites and then migrate to hcp given the similar stability of these sites (Table S7). The hcp → fcc activation energy show negligible dependence on H* coverage for coverages from 0.062 ML to 0.5 ML. At higher coverages, the hcp → fcc migration could not be simulated due to lateral repulsion from neighboring H* atoms forcing the fcc H* to spontaneously migrate back to the hcp site upon optimization. For the hcp → fourfold hollow activation energy dependence on H* coverage is also mostly negligible. Overall, all activation energies are sufficiently low that we can expect diffusion to occur at all coverages investigated for both pathways. At H* coverage > 0.5 ML, fourfold hollow sites start being occupied; hence we have investigated migration in between these sites, which are sufficiently close for H* to diffuse directly from one to the other (Figure 2a). The corresponding activation energy has been

calculated at 0.875 ML since these sites can be occupied only at high H* coverages and resulted to be 0.10 eV.

For the $(10\bar{1}0)$ surface we do not explore the migration pathway linking the most stable higher bridge sites, because H_2 dissociation was found to spontaneously lead to the most stable arrangement of H*. We instead focused on two other migration pathways and calculated the associated barriers (Table 2): higher bridge site → higher hollow site and higher hollow site → lower hollow site → higher hollow site (Figure 2b). The first pathway is important because up to 0.5 ML H* coverage only higher bridge sites are occupied but beyond this coverage a newly added H* adsorbs on a higher hollow site and forces a neighboring higher bridge H* to move to a higher hollow site. The second pathway is important as the migration between neighboring higher hollow sites can only occur via a lower hollow site. The higher bridge → higher hollow pathway was found to be essentially barrierless while the higher hollow → lower hollow pathway presents a more significant activation barrier for H* migration. That said, they are sufficiently small at all investigated H* coverages that a fast diffusion process should occur on this surface as well. Thus, overall, the most favorable arrangement of hydrogen atoms can be achieved on both the $(10\bar{1}1)$ and the $(10\bar{1}0)$ surface upon H_2 dissociation. Our results reporting a small effect of the H* coverage on the migration activation energy compare well with previously reported data for the Ru (0001) surface.[39]

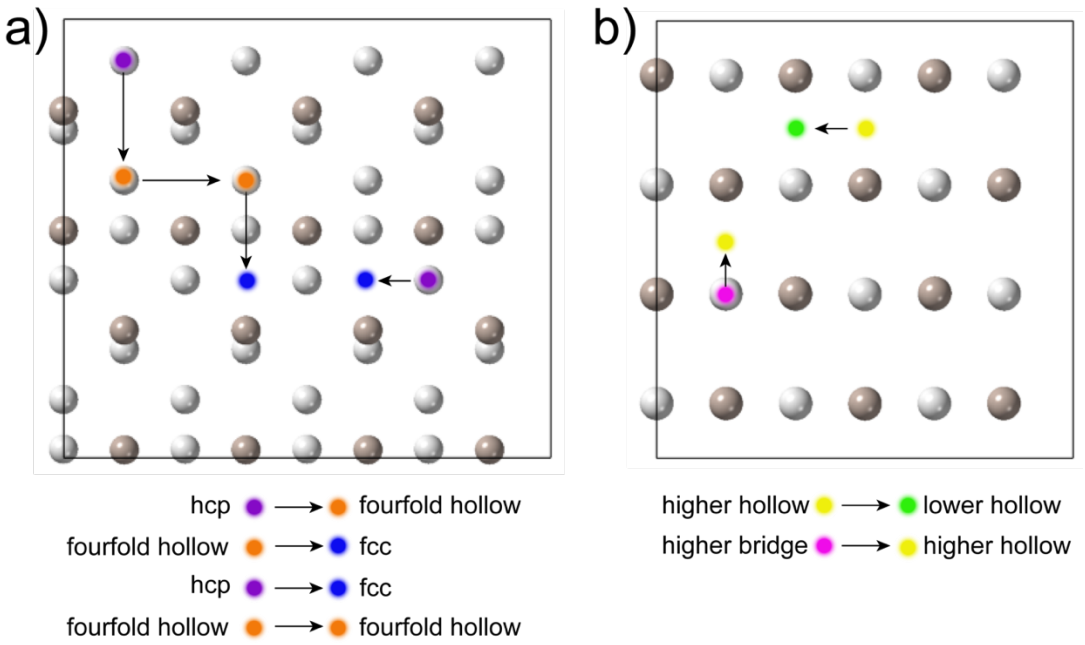

Figure 2: Adsorbed atomic hydrogen migration pathways involving all the sites within 0.1 eV stability from the most stable one on the (a) $(10\bar{1}1)$ surface and (b) $(10\bar{1}0)$ surface. Differently colored circles denote different sites on the surfaces as shown in figure legend. The figure shows the surface top views and the top Ru layer atoms are represented as dark grey spheres and the bottom Ru layer atoms as pale grey spheres.

Atomic hydrogen coverage [ML]	hcp → fcc activation energy [eV]	hcp → fourfold hollow activation energy [eV]	fourfold hollow → fcc activation energy [eV]
0.062	0.14 (0.16)	0.16 (0.22)	0.21 (0.17)
0.125	0.15 (0.17)	0.16 (0.22)	0.22 (0.18)
0.500	0.13 (0.15)	0.11 (0.18)	0.11 (0.06)
0.875	---	0.09 (0.16)	---

Table 1: Activation energies (eV) for relevant migration pathways of atomic hydrogen over the $(10\bar{1}1)$ surface as a function of hydrogen coverage. Values for the backward process are reported in brackets. Energies are reported at 0 K with ZPE corrections.

Atomic hydrogen coverage [ML]	higher bridge → higher hollow activation energy [eV]	higher hollow → lower hollow activation energy [eV]

0.083	0.00 (0.01)	0.14 (0.21)
0.250	0.01 (0.02)	0.19 (0.25)
0.583	0.06 (0.08)	---

Table 2: Activation energies (eV) for relevant migration pathways of atomic hydrogen over the $(10\bar{1}0)$ surface as a function of hydrogen coverage. Values for the backward process are reported in brackets. Energies are reported at 0 K with ZPE corrections.

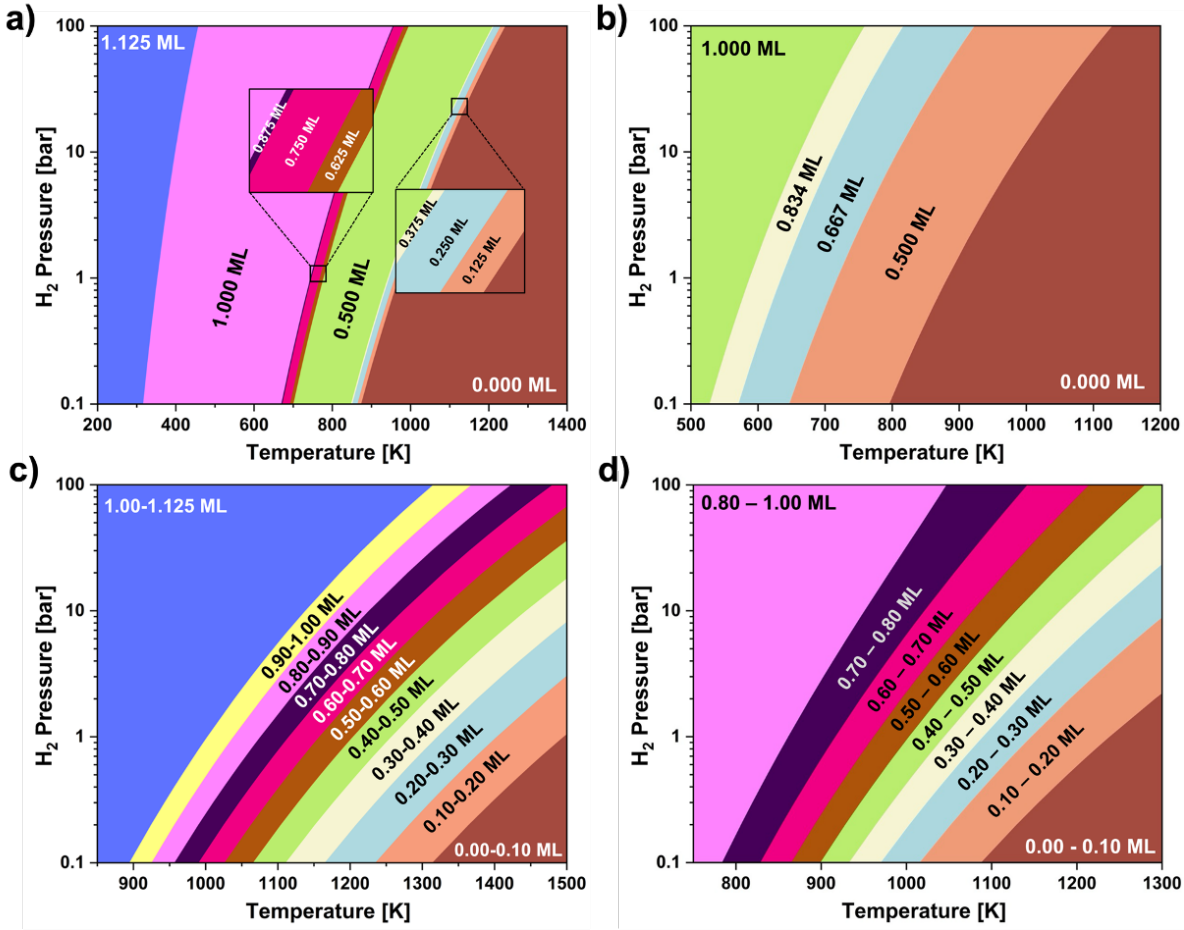

Figure 3: Ab initio thermodynamic surface phase diagrams showing the most stable atomic hydrogen coverage, expressed in terms of monolayers (MLs), on (a) the $(10\bar{1}1)$ surface and (b) the $(10\bar{1}0)$ surface generated via direct dissociation of H_2 gas under different temperature and H_2 pressure conditions. Kinetic surface phase diagrams showing the range of kinetically stable atomic hydrogen coverages on (c) the $(10\bar{1}1)$

surface and (d) the $(10\bar{1}0)$ surface under different temperature and H_2 pressure conditions.

In order to determine the expected H* coverage under different temperature and H_2 pressure conditions, we built a surface phase diagram according to ab-initio thermodynamics (Method section) for both the $(10\bar{1}1)$ surface (Figure 3a) and the $(10\bar{1}0)$ surface (Figure 3b); the phases displayed in these diagrams represent the most stable H* coverage at the given conditions. Both surfaces show that coverages lower than 1 ML are only stable at temperatures higher than 600 K under all H_2 pressures investigated (0.1 bar to 100 bar). This suggests that under catalytic conditions the two investigated surfaces are fully covered in H*. Given our finding that for the $(10\bar{1}1)$ surface H_2 dissociation is favorable even at H* coverage > 1 ML, we also checked the stability of H* coverages exceeding 1 ML on this surface. Interestingly we observe that different coverages show different stability ranges. The $(10\bar{1}1)$ thermodynamic surface phase diagram (Figure 3a) shows that all coverages investigated are stable under certain temperature and H_2 pressure conditions but the 0.5 ML, and the 1 ML ones have the largest stability range. On the other hand, coverages between 0.083 and 0.334 ML are not stable under any condition on the $(10\bar{1}0)$ surface, hence they are not observed in the phase diagram (Figure 3b). We can explain these different stability ranges based on the trend of ΔG_{Diss} in Figure 1. Indeed, when ΔG_{Diss} becomes significantly less favorable as the starting coverage increases (e.g., from 0.334 ML to 0.5 ML for the $(10\bar{1}0)$ surface, Figure 1) we observe a widening of the temperature stability range of the coverage formed by dissociating H_2 molecules up to the abrupt increase in ΔG_{Diss}. On the other hand, if no significant changes are observed in ΔG_{Diss} as the starting coverage increases, (e.g., downhill from 0 ML to 0.167 ML on the $(10\bar{1}0)$ surface, or almost flat from 0.250 ML to 0.375 ML on the $(10\bar{1}1)$ surface) the formed coverages are either not present or their temperature stability ranges are extremely narrow in the phase diagram.

In order to provide a complete analysis of the H* coverage stability on the investigated surfaces, we also accounted for the direct dissociation kinetics by creating kinetic phase diagrams (Figure 3c and 3d). Because the method used for the generation of these phase diagrams (Methods section) calculates the continuous variation of coverage with temperature rather than discrete coverages, we cannot report exact phase transitions between individual coverages; we instead report transitions between ranges of coverages. The kinetic phase diagrams show an increased stability of high coverages (0.8-1.0 ML) relative to the thermodynamic ones, with transitions to lower coverages only occurring at around 880 K for the $(10\bar{1}1)$ surface (Figure 3c) and 780 K for the $(10\bar{1}0)$ surface (Figure 3d). The increased stability of high coverages when including kinetic effects can be explained by the high affinity of the investigated surfaces towards atomic hydrogen, as reported by significantly lower reaction rates for associative desorption compared to the dissociative adsorption process (Tables S5 and S6 in the Supporting Information). Overall, the kinetic phase diagrams also confirm that under catalytic conditions the two investigated surfaces will be fully covered in H*.

Effect of hydrogen coverage on adsorption and dehydrogenation of butane

Ru nanoparticles have been used successfully for the catalytic hydrogenolysis of polyethylene. In order for the polymer chain to break down, the polymer must interact with the hydrogenated Ru surface. Therefore, to assess whether such interactions are favorable on the two Ru surfaces under study in this work, we investigated the adsorption of butane at catalytically relevant H* coverages. The interaction of polymeric chains with surfaces is known to occur via a train-loop-tail adsorption mode, meaning that only a small portion of the polymeric chain (i.e., the so called "train") directly interacts with the surface.[42] Recent molecular dynamics simulations have confirmed this behavior for Ru nanoparticles of the typical size used in hydrogenolysis experiments (1 – 3 nm)[2,3, 15,43] and have shown that the train

length distribution is centered around five carbon atoms.[44] This suggests that butane is a reasonable model of the adsorbed portion of the polymer that will undergo hydrogenolysis on small nanoparticles. Moreover, given the relatively small size of butane, we are able to use a smaller unit cell and maintain a reasonable computational cost. In typical hydrogenolysis experiments the catalyst is first reduced using hydrogen and then the polymer or alkane is introduced, eventually followed by more hydrogen to carry out the reaction.[45] Given the significant exposure to elevated H_2 pressure (above 10 bar) and temperatures (above 450 K) and based on our computed phase diagrams for the $(10\bar{1}1)$ and $(10\bar{1}0)$ surfaces (Figure 3), we expect both surfaces to be fully covered by H* when the polymer reacts at the surface. Thus, butane adsorption energy was evaluated on the fully H* covered surfaces, with the butane positioned on top of the H* layer (Figure S7), as well as on the bare surface as reference.

Surface	Butane adsorption energy at 0 ML H* coverage [eV]	Butane adsorption energy at 1 ML H* coverage [eV]
$(10\bar{1}1)$	-0.98	-0.56
$(10\bar{1}0)$	-1.07	-0.74

Table 3: Adsorption energies (eV) of butane at 0 monolayer (ML) and 1 ML of atomic hydrogen (H*) coverage on the $(10\bar{1}1)$ and $(10\bar{1}0)$ Ru surfaces. Energies are reported at 0 K with ZPE corrections.

At 0 ML of H* coverage, butane favorably adsorbs on both surfaces as indicated by the negative adsorption energies (Table 3). At 1 ML the adsorption energy remains negative meaning that interaction with the surface is still favorable, but it increases by about 0.4 eV on the $(10\bar{1}1)$ surface and 0.3 eV on the $(10\bar{1}0)$ surface. On both surfaces we tested a few different initial configurations of butane for each coverage. While at 0 ML there is a more pronounced difference in stability between different configurations (about 0.05 eV), at 1 ML all

configurations tested are essentially isoenergetic (maximum difference < 0.02 eV). This suggests that while the hydrogenated surface is still attractive, there are no specific chemical interactions but general dispersion interaction. A potentially more favorable adsorption route for butane on the fully covered surface may involve H* atoms recombining and desorbing as H_2 to leave empty surface sites for the polymer train to interact directly with the surface similarly to what was proposed for the hydrogen mediated ammonia decomposition.[46] However, this is unlikely to happen given that the dissociation energy of a single H_2 molecule even at H* coverage nearing 1 ML (Figure 1) is similar to the adsorption energy of butane on the bare surface; This indicates that there is no thermodynamic driving force for multiple H* atoms to desorb to allow butane to adsorb on empty surface sites.

Comparing results across the two surfaces, we notice that the adsorption energies on the $(10\bar{1}0)$ surface are consistently more favorable than on the $(10\bar{1}1)$ surface. This result can be explained on the bare surface by the higher surface energies calculated for the $(10\bar{1}0)$ surface (Table S4 in the Supporting Information) indicating lower stability and stronger driving force to interact with adsorbates. On the fully H* covered surfaces, the trend can be explained based on the alignment of the surface H*, which carry a partial negative charge (-0.17 |e| average for the H* on the $(10\bar{1}0)$ surface, and -0.20 |e| average for the H* on the $(10\bar{1}1)$ surface), with the hydrogens belonging to the adsorbed butane molecule, which carry a partial positive charge (0.03 |e| on averaged across all the butane hydrogens on both surfaces). On the $(10\bar{1}1)$ surface only two C-H bonds directly align with two H* (Figure S7) while on the $(10\bar{1}0)$ surface four C-H bonds pointing downwards are aligned with four H* (Figure S8).

Having established that butane favorably interacts with both surfaces even at 1 ML of H* coverage expected under experimental conditions, we move on to analyze the effect of the H* coverage on the dehydrogenation process, which is the first step in the hydrogenolysis mechanism and it is followed by C-C cleavage.[47] Both terminal and central C-C cleavage can

occur for butane (and polyethylene); here we focus on the dehydrogenation leading to terminal cleavage given that it is associated with the production of the unwanted product methane. The main mechanism for metal catalyzed alkane dehydrogenation proposed in the literature is a monomolecular (MM) mechanism (Figure 4a), in which one C-H bond breaks by interacting with bare Ru surface atoms.[15,48,49] This is a reasonable mechanism for these studies in which only the bare surface was modeled. Given our finding that these surfaces will be fully covered by hydrogen, we propose an alternative mechanism in which a H* combines with the H from the butane C-H bond being cleaved thus forming H_2 and freeing surface area for the alkyl radical adsorption (Figure 4b); we refer to this mechanism as the bimolecular (BM) mechanism.

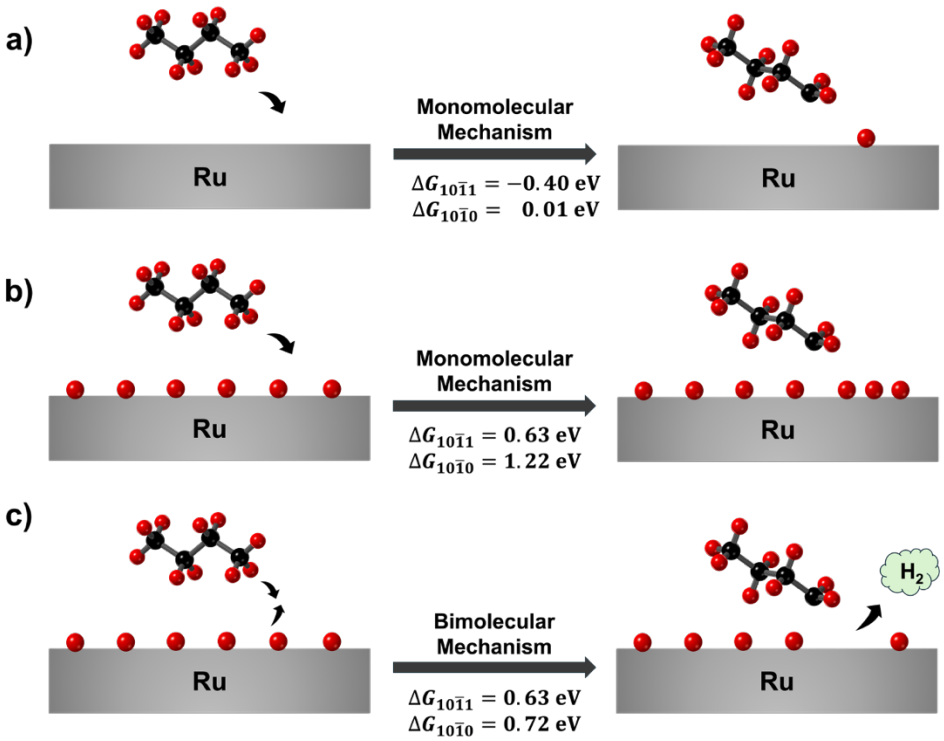

Figure 4: Schemes and associated reaction free energies for the monomolecular dehydrogenation of butane at (a) 0 monolayer (ML) and (b) 1 ML of hydrogen coverage and (c) bimolecular dehydrogenation of butane at 1 ML of hydrogen coverage. ZPE corrected reaction free energies for the Ru $(10\bar{1}1)$ and $(10\bar{1}0)$ surfaces evaluated at 473 K and 10 bar of H_2 pressure are reported below the reaction arrows. Black spheres

represent carbon atoms, red spheres represent hydrogen atoms, and the grey bar represents a generic Ru surface.

We start our analysis with the more established MM mechanism. Although the surfaces will both be fully covered by hydrogen under experimental conditions, we still calculated the dehydrogenation reaction energy at 0 ML of H* coverage as a point of reference. We found that the reaction is thermodynamically favored on the $(10\bar{1}1)$ surface ($\Delta G = -0.40\ eV$) and thermoneutral on the $(10\bar{1}0)$ ($\Delta G = 0.01\ eV$). Given that this reaction results in the formation of one H*, the more favorable reaction energy on the $(10\bar{1}1)$ surface can be simply explained by the stronger H* adsorption energy (Table S7 and S8) and more favorable H_2 dissociation (Figure 1) with respect to the $(10\bar{1}0)$ surface. In addition, we observed an attractive interaction between the adsorbed butyl radical and the H* on the $(10\bar{1}1)$ surface (Table S11 of the Supporting Information), which could further contribute to the more favorable reaction energy on this surface.

When the surfaces are fully covered, the H* and the radical resulting from the C-H cleavage in the MM mechanism (Figure 4b) have to adsorb on less stable vacant sites: namely the higher top sites for the butyl radical on both surfaces, and an interstitial position between a bridge and a higher hollow site for H* on the $(10\bar{1}0)$ and a bridge site on the $(10\bar{1}1)$. These sites will be fully surrounded by preadsorbed H*, thus possibly leading to large lateral repulsion. Not surprisingly, we find the dehydrogenation energies to be significantly higher relative to the 0 ML case. Once again, we observe that the reaction energies for the $(10\bar{1}1)$ surface are more favorable (although still positive) relative to the $(10\bar{1}0)$ surface. In addition to the attractive interaction between the butyl radical and the H* on the $(10\bar{1}1)$ surface discussed above, this can be explained based on our finding previously presented that H_2 dissociation at 1 ML is not favorable on the $(10\bar{1}0)$ surface while it is still favorable on the $(10\bar{1}1)$ surface. As an alternative to the butyl radical and H* having to adsorb on the fully

hydrogenated surfaces, one could hypothesize that multiple H* atoms might recombine and desorb to leave space for the radical. However, this is highly unlikely given that the dissociation energy of just one H_2 molecule at high coverage is significantly more favorable than the MM dehydrogenation reaction energy even at 0 ML, indicating no thermodynamic driving force for H* atoms to desorb to allow this reaction to happen. We thus conclude that H* is poisoning the surface by blocking the available adsorption sites for the alkyl radicals. Similar poisoning effects have been reported for other reactions involving hydrogen and Ru nanoparticles.[46,50]

The computed reaction free energies for the BM mechanism at 1 ML of H* coverage (Figure 4c) are positive for both the $(10\bar{1}1)$ and $(10\bar{1}0)$ surfaces. In particular, the reaction free energy for the $(10\bar{1}1)$ surface (0.63 eV) is the same as the one computed for the MM mechanism at 1 ML of H* coverage, suggesting that the two dehydrogenation mechanisms will compete on this surface. On the other hand, the BM mechanism for the fully hydrogenated $(10\bar{1}0)$ surface is significantly more favorable than the MM mechanism (0.5 eV lower free energy), meaning that the BM mechanism will be the main dehydrogenation route on this surface. The preference for the BM mechanism for the $(10\bar{1}0)$ surface can be explained by the fact that the desorption of only one H* from the surface, though energetically unfavorable, is compensated by the decrease in co-adsorbing H* lateral interactions as well as by the gain of rotational and translational mode of the desorbed H_2 molecule. While the latter is a common effect for both surfaces, the decrease in lateral interactions is more pronounced on the $(10\bar{1}0)$ surface because the adjacent higher hollow H* adsorption sites are 0.5 Å closer to each other than any adjacent site pair on the $(10\bar{1}1)$ surface. Overall, we expect that butane dehydrogenation via the BM mechanism would compete with the MM mechanism on the $(10\bar{1}1)$ surface while it will dominate the reactivity of butane dehydrogenation on the $(10\bar{1}0)$ surface. More generally, both mechanisms have positive reaction energies suggesting that the

hydrogenation step will be slow on these fully hydrogenated surfaces and the observed reactivity of Ru nanoparticles is mainly due to the significant exposure of the (0001) surface.

Conclusions

In this study, we employed periodic DFT calculations to investigate the interaction of molecular and atomic hydrogens with the Ru $(10\bar{1}1)$ and Ru $(10\bar{1}0)$ surfaces, a limited area of research thus far. The promising activities of these Ru surfaces in various catalytic processes encouraged us to explore their potential role in plastic hydrogenolysis, a process that uses large hydrogen pressures and moderate temperatures to cleave polymeric chains and convert polyolefin plastic waste into useful chemicals. Understanding how hydrogen interacts with the surface and affects its reactivity towards the plastic chains is crucial for ultimately unraveling the reaction mechanism, predicting the product distribution, and design improved catalyst.

We started our investigation by identifying the most favorable sites for atomic hydrogen adsorption on the two Ru surfaces, namely hcp and fcc sites on the $(10\bar{1}1)$ surface, and higher hollow and higher bridge sites on the $(10\bar{1}0)$ surface. We found that H_2 spontaneously dissociates on all the investigated sites except for the higher top sites on both surfaces. This behavior is very different from the most stable surface of Ru, the (0001), on which H_2 was found to molecularly adsorb in a previous work. Furthermore, our results show that atomic hydrogen can easily migrate on the surface to achieve the most stable arrangement at different coverages. Using ab-initio thermodynamics and microkinetic modeling, we then developed phase diagrams to predict the atomic hydrogen coverage in a wide range of temperature (200 K to 1500 K) and H_2 pressure (0.1 bar to 100 bar). The phase diagrams indicate that the investigated Ru surfaces will be fully covered with hydrogen under the typical catalytic conditions (473 K – 523 K, and 10 bar – 90 bar of H_2 pressure). Having established the level of hydrogenation of these surfaces under experimental conditions, we moved on to explore how this aspect affects the polymer hydrogenolysis. To this end, we used butane to model the

portion of the polyethylene chain directly interacting with the surface. In particular, we studied the adsorption and dehydrogenation of butane, the two steps needed for C-C cleavage to occur. We found that, despite being less favorable, the adsorption can occur on both surfaces even when fully hydrogenated. We then explored the energetics of two possible mechanisms for butane dehydrogenation, namely the monomolecular and the bimolecular mechanism. In the former, one butane C-H bond breaks by interacting with the surface, leading to the formation of co-adsorbed butyl radical and hydrogen atom. In the bimolecular one, an adsorbed hydrogen mediates the interaction between the butane C-H bond and the surface, leading to the formation of an adsorbed butyl radical and an H_2 molecule. Our computed reaction free energies suggest that the monomolecular mechanism is favorable on the bare surface but the bimolecular one is preferred on the fully hydrogenated surfaces, especially for the $(10\bar{1}0)$ surface. However, the reaction free energies are positive, indicating that the hydrogenation process will be slow.

Overall, our investigation suggests that the Ru $(10\bar{1}1)$ and $(10\bar{1}0)$ surfaces are unlikely to be particularly active towards polyolefin hydrogenolysis trains but they are very effective for H_2 splitting. Thus, we hypothesize that, in a typical nanoparticle exposing multiple low-index facets along with the most stable (0001) facet, the Ru $(10\bar{1}1)$ and $(10\bar{1}0)$ surfaces will split H_2 and store atomic hydrogen. This stored hydrogen can then diffuse to other exposed surfaces, where the polyolefin cleavage is occurring, as needed; migration of atomic hydrogen across facets is a well-known phenomenon for Ru.[51] However, more work is needed to elucidate the polyethylene hydrogenolysis mechanism on less hydrogenated facet exposed in typical nanoparticles, such as the most stable (0001) facet. Work is currently underway in our group to investigate these aspects.

Acknowledgments

The research by F.C. is supported by a University International Postgraduate Award (UIPA) scholarship from UNSW Sydney. This work was supported by the Australian Research Council

Discovery Project DP230100596. We are grateful for the computational resources and services from the National Computational Infrastructure (NCI), provided by the Australian government under the National Computational Merit Allocation Scheme and the computational cluster Katana supported by the Research Technology Services at UNSW Sydney. Prof Richard Tilley, Prof Justin Gooding, Prof Julie Rorrer, Michele Pettini, and Marzia Cavallo are acknowledged for their helpful suggestions during this project.

References

(1) Humphreys, J.; Lan, R.; Tao, S. Development and Recent Progress on Ammonia Synthesis Catalysts for Haber–Bosch Process. *Adv Energ Sust Res* **2021**, *2* (1), 2000043.

(2) Celik, G.; Kennedy, R. M.; Hackler, R. A.; Ferrandon, M.; Tennakoon, A.; Patnaik, S.; Lapointe, A. M.; Ammal, S. C.; Heyden, A.; Perras, F. A.; Pruski, M.; Scott, S. L.; Poeppelmeier, K. R.; Sadow, A. D.; Delferro, M. Upcycling Single-Use Polyethylene into High-Quality Liquid Products. *ACS Cent Sci* **2019**, *5* (11), 1795–1803.

(3) Rorrer, J. E.; Troyano-Valls, C.; Beckham, G. T.; Román-Leshkov, Y. Hydrogenolysis of Polypropylene and Mixed Polyolefin Plastic Waste over Ru/C to Produce Liquid Alkanes. *ACS Sustain Chem Eng* **2021**, *9* (35), 11661–11666.

(4) Rorrer, J. E.; Ebrahim, A. M.; Questell-Santiago, Y.; Zhu, J.; Troyano-Valls, C.; Asundi, A. S.; Brenner, A. E.; Bare, S. R.; Tassone, C. J.; Beckham, G. T.; Román-Leshkov, Y. Role of Bifunctional Ru/Acid Catalysts in the Selective Hydrocracking of Polyethylene and Polypropylene Waste to Liquid Hydrocarbons. *ACS Catal* **2022**, *12* (22), 13969–13979.

(5) Nakagawa, Y.; Oya, S. I.; Kanno, D.; Nakaji, Y.; Tamura, M.; Tomishige, K. Regioselectivity and Reaction Mechanism of Ru-Catalyzed Hydrogenolysis of Squalane and Model Alkanes. *ChemSusChem* **2017**, *10* (1), 189–198.

(6) Tamura, M.; Miyaoka, S.; Nakaji, Y.; Tanji, M.; Kumagai, S.; Nakagawa, Y.; Yoshioka, T.; Tomishige, K. Structure-Activity Relationship in Hydrogenolysis of Polyolefins over Ru/Support Catalysts. *Appl Catal B* **2022**, *318*, 121870.

(7) Chen, L.; Zhu, Y.; Meyer, L. C.; Hale, L. V; Le, T. T.; Karkamkar, A.; Lercher, J. A.; Gutiérrez, O. Y.; Szanyi, J. Effect of Reaction Conditions on the Hydrogenolysis of Polypropylene and Polyethylene into Gas and Liquid Alkanes. *React Chem Eng* **2022**, *7*, 844–854.

(8) Wang, C.; Xie, T.; Kots, P. A.; Vance, B. C.; Yu, K.; Kumar, P.; Fu, J.; Liu, S.; Tsilomelekis, G.; Stach, E. A.; Zheng, W.; Vlachos, D. G. Polyethylene Hydrogenolysis at Mild Conditions over Ruthenium on Tungstated Zirconia. *JACS Au* **2021**, *1* (9), 1422–1434.

(9) Poerwoprajitno, A. R.; Gloag, L.; Watt, J.; Cheong, S.; Tan, X.; Lei, H.; Tahini, H. A.; Henson, A.; Subhash, B.; Bedford, N. M.; Miller, B. K.; O'Mara, P. B.; Benedetti, T. M.; Huber, D. L.; Zhang, W.; Smith, S. C.; Gooding, J. J.; Schuhmann, W.; Tilley, R. D. A Single-Pt-Atom-on-Ru-Nanoparticle Electrocatalyst for CO-Resilient Methanol Oxidation. *Nat Catal* **2022**, *5* (3), 231–237.
(10) Poerwoprajitno, A. R.; Gloag, L.; Benedetti, T. M.; Cheong, S.; Watt, J.; Huber, D. L.; Gooding, J. J.; Tilley, R. D. Formation of Branched Ruthenium Nanoparticles for Improved Electrocatalysis of Oxygen Evolution Reaction. *Small* **2019**, *15* (17), 1804577.
(11) Wang, F.; Li, C.; Zhang, X.; Wei, M.; Evans, D. G.; Duan, X. Catalytic Behavior of Supported Ru Nanoparticles on the {1 0 0}, {1 1 0}, and {1 1 1} Facet of CeO2. *J Catal* **2015**, *329*, 177–186.
(12) Cui, X.; Li, Z.; Jang, H.; Kim, M. G.; Liu, S.; Hou, L.; Liu, X. Anomalous Dominated (100) Index Facet Endows Ruthenium Nanoparticles with Accelerated Alkaline Hydrogen Evolution. *Inorg Chem Front* **2024**, *11* (5), 1552–1560.
(13) Du, X.; Lang, Y.; Cao, K.; Yang, J.; Cai, J.; Shan, B.; Chen, R. Bifunctionally Faceted Pt/Ru Nanoparticles for Preferential Oxidation of CO in H2. *J Catal* **2021**, *396*, 148–156.
(14) Nanba, Y.; Ishimoto, T.; Koyama, M. Structural Stability of Ruthenium Nanoparticles: A Density Functional Theory Study. *J Phys Chem C* **2017**, *121* (49), 27445–27452.
(15) Xie, T.; Wittreich, G. R.; Vlachos, D. G. Multiscale Modeling of Hydrogenolysis of Ethane and Propane on Ru(0001): Implications for Plastics Recycling. *Appl Catal B* **2022**, *316*, 121597.
(16) Zhao, M.; Xia, Y. Crystal-Phase and Surface-Structure Engineering of Ruthenium Nanocrystals. *Nat Rev Mater* **2020**, *5* (6), 440–459.
(17) Li, L.; Tian, F.; Qiu, L.; Wu, F.; Yang, W.; Yu, Y. Recent Progress on Ruthenium-Based Electrocatalysts towards the Hydrogen Evolution Reaction. *Catalysts* **2023**, *13* (12), 1497.
(18) Colasuonno, F.; Lessio, M. Thermodynamic and Kinetic Insights into Hydrogen Adsorption and Dissociation on the Ru (0001) Surface under STM and Catalytic Conditions. *J Phys Chem C* **2023**, *127* (49), 23645–23653.
(19) Tran, R.; Xu, Z.; Radhakrishnan, B.; Winston, D.; Sun, W.; Persson, K. A.; Ong, S. P. Surface Energies of Elemental Crystals. *Sci Data* **2016**, *3* (1), 160080.
(20) Wang, L.-L.; Yu, Z.-Y.; Lu, T.-B. Recent Advances of Ruthenium-Based Materials for Acidic Oxygen Evolution Reaction: From Catalyst Design to Proton Exchange Membrane Water Electrolysers. *J Mater Chem A Mater* **2024**, *12* (35), 23297–23314.
(21) Chen, L.; Li, Y.; Liang, X. Ar/H $_2$ /O $_2$ -Controlled Growth Thermodynamics and Kinetics to Create Zero-, One-, and Two-Dimensional Ruthenium Nanocrystals towards Acidic Overall Water Splitting. *Adv Funct Mater* **2021**, *31* (11), 2007344.
(22) Watt, J.; Yu, C.; Chang, S. L. Y.; Cheong, S.; Tilley, R. D. Shape Control from Thermodynamic Growth Conditions: The Case of Hcp Ruthenium Hourglass Nanocrystals. *J Am Chem Soc* **2013**, *135* (2), 606–609.
(23) Manabe, R.; Nakatsubo, H.; Gondo, A.; Murakami, K.; Ogo, S.; Tsuneki, H.; Ikeda, M.; Ishikawa, A.; Nakai, H.; Sekine, Y. Electrocatalytic Synthesis of Ammonia by Surface Proton Hopping. *Chem Sci* **2017**, *8* (8), 5434–5439.
(24) Kresse, G.; Hafner, J. Ab. Initio Molecular Dynamics for Liquid Metals. *Phys Rev B* **1993**, *47* (1), 558–561.
(25) Kresse, G.; Furthmü, J. Efficient Iterative Schemes for Ab Initio Total-Energy Calculations Using a Plane-Wave Basis Set. *Phys Rev B* **1996**, *54* (16), 11169–11186.

(26) Kresse, G.; Furthmiiller B ', J. Efficiency of Ab-Initio Total Energy Calculations for Metals and Semiconductors Using a Plane-Wave Basis Set. *Comput Mater Sci* **1996**, *6* (1), 15–50.
(27) Perdew, J. P.; Burke, K.; Ernzerhof, M. Generalized Gradient Approximation Made Simple. *Phys Rev L* **1996**, *77* (18), 3865–3868.
(28) Grimme, S.; Antony, J.; Ehrlich, S.; Krieg, H. A Consistent and Accurate Ab Initio Parametrization of Density Functional Dispersion Correction (DFT-D) for the 94 Elements H-Pu. *J Chem Phys* **2010**, *132* (15), 154104.
(29) Grimme, S.; Ehrlich, S.; Goerigk, L. Effect of the Damping Function in Dispersion Corrected Density Functional Theory. *J Comput Chem* **2011**, *32*, 1456–1465.
(30) Kresse, G.; Joubert, D. From Ultrasoft Pseudopotentials to the Projector Augmented-Wave Method. *Phys Rev B* **1999**, *59* (3), 1758–1775.
(31) Henkelman, G.; Uberuaga, B. P.; Jónsson, H. Climbing Image Nudged Elastic Band Method for Finding Saddle Points and Minimum Energy Paths. *J Chem Phys* **2000**, *113* (22), 9901–9904.
(32) Henkelman, G.; Jónsson, H. A Dimer Method for Finding Saddle Points on High Dimensional Potential Surfaces Using Only First Derivatives. *J Chem Phys* **1999**, *111* (15), 7010–7022.
(33) Sholl, D. S.; Steckel, J. A. Equilibrium Phase Diagrams FromAb Initio Thermodynamics. In *Density Functional Theory*; John Wiley & Sons, Inc., 2009; pp 163–177.
(34) López, M.; Morales-García, Á.; Viñes, F.; Illas, F. Thermodynamics and Kinetics of Molecular Hydrogen Adsorption and Dissociation on MXenes: Relevance to Heterogeneously Catalyzed Hydrogenation Reactions. *ACS Catal* **2021**, *11* (21), 12850–12857.
(35) Johansson, M.; Lytken, O.; Chorkendorff, I. The Sticking Probability for H2 on Some Transition Metals at a Hydrogen Pressure of 1bar. *J Chem Phys* **2008**, *128* (3), 034706–2.
(36) Feulner, P.; Menzel, D. The Adsorption of Hydrogen on Ruthenium (001): Adsorption States, Dipole Moments and Kinetics of Adsorption and Desorption. *Surf Sci* **1985**, *154* (2–3), 465–488.
(37) Filot, I. A. W. *Introduction to Microkinetic Modeling*; Technische Universiteit Eindhoven, 2018.
(38) Konda, S. K.; Chen, A. Palladium Based Nanomaterials for Enhanced Hydrogen Spillover and Storage. *Mater Today* **2016**, *19* (2), 100–108.
(39) Greeley, J.; Mavrikakis, M. Surface and Subsurface Hydrogen: Adsorption Properties on Transition Metals and near-Surface Alloys. *J Phys Chem B* **2005**, *109* (8), 3460–3471.
(40) Chou, M. Y.; Chelikowsky, J. R. First-Principles Study of Hydrogen Adsorption on Ru(0001): Possible Occupation of Subsurface Sites. *Phys Rev Lett* **1987**, *59* (15), 1737–1740.
(41) Kostov, K. L.; Widdra, W.; Menzel, D. Hydrogen on Ru(0 0 1) Revisited: Vibrational Structure, Adsorption States, and Lateral Coupling. *Surf Sci* **2004**, *560* (1–3), 130–144.
(42) Scheutjens, J. M. H. M.; Fleer, G. J. Statistical Theory of the Adsorption of Interacting Chain Molecules. 2. Train, Loop, and Tail Size Distribution. *J Phys Chem* **1980**, *84* (2), 178–190.
(43) Rorrer, J. E.; Beckham, G. T.; Román-Leshkov, Y. Conversion of Polyolefin Waste to Liquid Alkanes with Ru-Based Catalysts under Mild Conditions. *JACS Au* **2020**, *1*, 8–12.

(44) Zare, M.; Kots, P. A.; Hinton, Z. R.; Epps, T. H.; Korley, L. T. J.; Caratzoulas, S.; Vlachos, D. G. Effect of Reaction Media on Hydrogenolysis of Polyethylene Plastic Waste: Polymer-Surface Interactions in Small Alkane/Polymer Blends. *Appl Catal B* **2024**, *351*, 123969.
(45) Musa, A.; Jaseer, E. A.; Barman, S.; Garcia, N. Review on Catalytic Depolymerization of Polyolefin Waste by Hydrogenolysis: State-of-the-Art and Outlook. *Energ Fuel* **2024**, *38* (3), 1676–1691.
(46) Beck, A.; Marlowe, J.; Gordon, M. J.; Christopher, P. Is There a Discernible Photochemical Effect Beyond Heating for Visible Photon-Mediated NH_3 Decomposition over Ru/Al_2O_3 ? *J Phys Chem C* **2024**, *128* (21), 8590–8600.
(47) Sinfelt, J. H. Catalytic Hydrogenolysis on Metals. *Catal Letters* **1991**, *9* (3–4), 159–171.
(48) Hibbitts, D. D.; Flaherty, D. W.; Iglesia, E. Effects of Chain Length on the Mechanism and Rates of Metal-Catalyzed Hydrogenolysis of n-Alkanes. *J Phys Chem C* **2016**, *120* (15), 8125–8138.
(49) Islam, M. M.; Catlow, C. R. A.; Roldan, A. Mechanistic Pathways for the Dehydrogenation of Alkanes on Pt(111) and Ru(0001) Surfaces. *ChemCatChem* **2024**.
(50) García-Antón, J.; Axet, M. R.; Jansat, S.; Philippot, K.; Chaudret, B.; Pery, T.; Buntkowsky, G.; Limbach, H. Reactions of Olefins with Ruthenium Hydride Nanoparticles: NMR Characterization, Hydride Titration, and Room-Temperature C - C Bond Activation. *Angew Chem Int Ed* **2008**, *47* (11), 2074–2078.
(51) Arena, M. V.; Westre, E. D.; Brown, D. E.; Kutzner, J.; George, S. M. Surface Diffusion of Hydrogen on a Stepped Ru(001) Surface. *Surf Sci* **1995**, *325* (1–2), 151–162.